CO 2 outperforms KOH as an activator for high-rate supercapacitors in aqueous electrolyte

J. Castro-Gutiérrez, R.L.S. Canevesi, M. Emo, M.T. Izquierdo, A. Celzard, Vanessa Fierro

CO_2 outperforms KOH as an activator for high-rate supercapacitors in aqueous electrolyte

Castro-Gutiérrez, J.[1], Canevesi, R. L. S.[1], Emo, M.[2], Izquierdo, M. T.[3], Celzard, A.[1], Fierro, V.[1,*]

[1] Université de Lorraine, CNRS, IJL, 88000 Epinal, France

[2] Université de Lorraine, CNRS, IJL, 54011 Nancy, France

[3] Instituto de Carboquímica (ICB-CSIC), Miguel Luesma Castán 4, E-50018, Zaragoza, Spain

* Corresponding author: Vanessa Fierro: vanessa.fierro@univ-lorraine.fr

Abstract

Although high-surface area activated carbons used as supercapacitor (SC) electrodes are frequently produced by KOH activation, this study shows that, when aqueous electrolytes are used, CO_2 activation is a better choice from the point of view of SC performance, environment and economy. Ordered mesoporous carbons (OMCs) produced by a mechanochemical synthesis method from mimosa tannin are activated with KOH to use these materials as electrodes for SCs. A comparative analysis of the same OMCs but activated with CO_2 is presented to examine the effect of the activation process on materials performance. KOH-activated materials exhibit good electrochemical performance at low charging rates, reaching specific cell capacitance values of 49 F g^{-1} at 0.5 A g^{-1}, however, restricted access to microporosity and low water affinity water reduces their performance at high charging rates. In contrast, the best performing CO_2-activated material can retain 81 % of capacitance at 20 A g^{-1}, compared to 25 % for a KOH-activated OMC with similar properties and tested under the same conditions. A thorough review of the open literature suggests that CO_2 activation would produce materials with a suitable combination of pore network connectivity and water affinity, resulting in SCs with high rate capability in an aqueous electrolyte. These conclusions were drawn by judiciously integrating the analysis of: (i) the hysteresis loop scanning of N_2 adsorption-desorption isotherms; and (ii) water adsorption isotherms as tools to more accurately assess the pore network connectivity and water affinity of the materials, which are not generally considered when studying SC performance.

Highlights

- Pore connectivity and water affinity control the performance of SCs
- Scanning the N_2 hysteresis loop allows the assessment of pore connectivity
- Poor connectivity and hydrophobicity of KOH-activated OMCs hinder SC performance
- Good connectivity and hydrophilicity of CO_2-activated OMCs enhance SC performance
- CO_2 activation is better in terms of SC performance and sustainability

Keywords: Supercapacitors; Ordered mesoporous carbons; Pore connectivity; Water affinity; Activated carbons, Tannins

Word count: 8296

Abbreviations

2D-NLDFT HS	2D Non-local density functional theory for heterogeneous surface
AC	Activated carbon
CO_2-AC	CO_2-activated carbon
CV	Cyclic voltammetry
EA	Elemental analysis
EDL	Electric double layer
EDR	Equivalent distributed resistance
EIS	Electrochemical impedance spectroscopy
GCD	Galvanostatic charge-discharge
KOH-AC	KOH-activated carbon
MF	Middle frequencies
OMC	Ordered mesoporous carbon
PSD	Pore size distribution
SC	Supercapacitor
SWAMM	Surfactant-water-assisted mechanochemical mesostructuration
TEM	Transmission electron microscopy
XPS	X-ray photoelectron spectroscopy
XRD	X-ray diffraction

Nomenclature

$(p/p_0)_{des}$	Starting relative pressure of the scanned desorption branches [dimensionless]
Δt_{12}	Discharge time from GCD measurements [s]
ΔV	Potential window [V]
A_{BET}	Area calculated using the Brunauer–Emmett–Teller theory [$m^2\ g^{-1}$]
BO	Burn-off [%]
$C_{0.01}$	Real part of the complex capacitance at 0.01 Hz [F]
C_{cell}	Specific cell capacitance [$F\ g^{-1}$]
CE	Coulombic efficiency [dimensionless]
$C_{e,BET}$	Specific electrode capacitance normalized by BET area [$F\ m^{-2}$]
CL	Carbon load [$mg\ cm^{-2}$]
C_r	Real part of the complex capacitance [F]
C_{ret}	Capacitance retention [%]
dV/dt	Slope of the discharge curve obtained from GCD measurements [$V\ s^{-1}$]
E	Specific energy [$Wh\ kg^{-1}$]
f	Frequency [Hz]
f_{knee}	Knee frequency [Hz]
I	Specific applied current [$A\ g^{-1}$]
I_{ap}	Applied current [A]
I_{meas}	Measured current [A]
iR	Potential drop [V]
m	Mass of active material in the two electrodes of the assembled SC [g]
O/S_{NLDFT}	Surface concentration of oxygen groups [$\mu mol\ m^{-2}$]
$OIII/S_{NLDFT}$	Surface concentration of carboxylic groups [$\mu mol\ m^{-2}$]
OMC-CO_2-*t*	OMC activated using CO_2 during t = 15 – 120 minutes
OMC-*x*-*r*	OMC material activated by impregnation or physical mixing (x = *imp* or *pm*, respectively) with KOH using a KOH/OMC mass ratio of r = 3 – 8
P	Specific power [$W\ kg^{-1}$]
p/p_0	Relative pressure [dimensionless]
s	Scan rate [$mV\ s^{-1}$]
S_{NLDFT}	Surface area calculated by applying the 2D-NLDF HS theory [$m^2\ g^{-1}$]
$V_{>5nm}$	Mesopore volume in the 5 – 50 nm range [$cm^3\ g^{-1}$]
V_{2-5nm}	Mesopore volume in the 2 – 5 nm range [$cm^3\ g^{-1}$]
V_{meso}	Total mesopore volume [$cm^3\ g^{-1}$]
$V_{s\mu}$	Supermicropore volume [$cm^3\ g^{-1}$]
V_{tot}	Total pore volume [$cm^3\ g^{-1}$]
$V_{u\mu}$	Ultramicropore volume [$cm^3\ g^{-1}$]
w	Pore width [nm]
$w_{av,\mu}$	Average micropore width [nm]
$w_{av,meso}$	Average mesopore width [nm]
$w_{av,s\mu}$	Average supermicropore width [nm]
$w_{av,u\mu}$	Average ultramicropore width [nm]
Z	Complex impedance [Ω]
Z_i	Imaginary part of the complex impedance [Ω]
Z_r	Real part of the complex impedance [Ω]

1. Introduction

Supercapacitors (SCs) are devices that store energy through the creation of an electric double layer (EDL) caused by the accumulation of ions on the electrode surface. Since the EDL mechanism does not involve Faradaic reactions, SCs can deliver the stored energy at high power outputs. Hierarchical porous carbons with porous structures consisting of micropores and narrow mesopores are suitable for use as electrodes for SCs since the micropores provide multiple charge storage sites while the mesopores promote ion diffusion, thereby improving their electrochemical performance, especially at high charging rates [1]. In particular, ordered mesoporous carbons (OMCs) have attracted interest in the field of electrochemical applications due to their tunable pore size and structure. They can be synthesized by hard- or soft-template methods using a variety of carbon precursors. Resorcinol and phenol, both of petrochemical origin, are usually employed as carbon precursors in the production of OMCs. However, the use of biosourced precursors such as sucrose, lignin, phloroglucinol, β-cyclodextrin extracted from starch, or tannin is becoming more common [2–8]. The final physicochemical properties of the OMCs change significantly depending on the choice of precursor and synthesis method. Therefore, materials with BET areas ranging from ~300 to ~3000 $m^2\ g^{-1}$ and pore volumes ranging from ~0.4 to ~4 $cm^3\ g^{-1}$ can be found [9,10].

Efforts to increase the capacitance and thus the amount of energy stored in carbon-based SCs are primarily focused on increasing the surface area by further developing the porosity of the synthesized materials through a physical or chemical activation process [11,12]. Again, the properties of activated carbons (ACs) depend on different factors such as carbon precursor, activating agent, or temperature, among others. Nevertheless, chemical activation has been shown to generally produce materials with surface areas sometimes greater than 2000 $m^2\ g^{-1}$, while physical activation achieves a maximum of ~1800 $m^2\ g^{-1}$ [11]. The activation process also modifies the surface chemistry of the materials, and ACs often contain oxygen functional

groups that can lead to pseudocapacitance contributions further increasing the capacitance at low charging rates. Moreover, it is frequently reported that surface functionalities can also improve the wettability (or water affinity) of carbon materials [2,12–20], which would facilitate ion diffusion and improve surface accessibility, both of which affect the SC performance in aqueous electrolytes at low and high charging rates. The water affinity of carbon materials has been evaluated by determining water adsorption isotherms [21–26]. It has been shown that water adsorption at low relative pressures (below 0.2 – 0.4) is highly dependent on the presence of oxygen functional groups acting as primary adsorption sites. These adsorption sites promote the formation and growth of clusters, and the eventual filling of micro- and mesopores, if any, at higher relative pressures [21,22]. Since a graphitic surface has a weak interaction with water molecules, the presence of oxygen functional groups may explain a greater water adsorption at low relative pressures. Their type and amount would provide a good indication of the water affinity of carbon materials, *i.e.*, their hydrophilicity or hydrophobicity [21,24–26]. Although these methods for assessing the wettability of carbon materials are already available, to the authors' knowledge, they are not used to relate the affinity for water to the performance of the materials as electrodes for SCs.

In this study, the textural properties of chemically and physically activated OMCs are thoroughly characterized and compared. Mimosa tannin, a non-toxic, inexpensive, abundant and commercially available polyphenolic molecule extracted from the bark of *Acacia mearnsii* trees, was used as a carbon precursor to produce OMCs through a surfactant-water-assisted mechanochemical mesostructuration (SWAMM) soft-templating method. The reactivity of mimosa tannin, similar to that of resorcinol, makes it possible to use it as an alternative to other precursors of petrochemical origin. In addition, this biosourced precursor can auto-condense, allowing resins to be obtained without the need of hazardous crosslinkers such as formaldehyde. Thus, the SWAMM method is a fast, green and one-pot method that

involves only the mixing of tannin with a pore-directing agent and small amounts of water in a single step inside a ball mill. The formed mesophase is then directly subjected to carbonization to produce OMCs with a 2D hexagonal structure [27]. Chemical activation was performed using KOH, one of the most commonly used activation agents in the literature, as described in many reviews and their references [9,11,14,28–36]. Based on these literature reports, two methods of KOH-incorporation routes were tested, namely impregnation with aqueous KOH solution and direct physical mixing of KOH pellets with the OMC. The obtained materials were then directly compared to physically activated OMCs from a previous study by our group, where CO_2 was used to activate the same type of tannin-derived OMCs produced by the SWAMM method [37]. For the textural properties, not only the surface area and porosity evolution were analyzed, but the connectivity of the pore network was also studied by scanning the hysteresis loops of N_2 adsorption-desorption isotherms. In addition, water adsorption isotherms were obtained for both types of materials, *i.e.*, KOH- or CO_2-activated OMCs, to evaluate their affinity for water and its relationship with their micropore size and oxygen surface functional groups. The results of these analyzes were used to explain the effect of the different activation processes on the electrochemical performance in an aqueous electrolyte (1 M H_2SO_4) of symmetric SCs using the activated OMCs as electrodes. Finally, a comparison with literature data on KOH- and CO_2-activated carbon materials, tested under similar conditions, suggests that CO_2 activation leads to materials with an appropriate combination of textural properties, pore network connectivity, and water affinity. These features enhance ion diffusion and surface accessibility, thus resulting in SC devices with high rate capability in an aqueous electrolyte (H_2SO_4).

2. Experimental

Materials. Mimosa tannin, commercially available under the name Fintan OP, was kindly provided by SilvaChimica (St Michele Mondovi, Italy). Pluronic® F127, KOH, carbon black, PTFE (60 wt.% suspension in water) and 1 M H_2SO_4 aqueous solution were all purchased from Sigma-Aldrich and used as received. In addition, 37 wt.% HCl aqueous solution, also from Sigma-Aldrich, was used to prepare 1 M HCl aqueous solution.

Synthesis. The ordered mesoporous carbon (OMC) was synthesized by the SWAMM method [27]. In a typical synthesis, mimosa tannin (T) and Pluronic® F27 (P) were ground together with water (W) in a planetary mill (PM 100, agate bowl and balls, Retsch), using a T:P:W mass ratio of 2:0.75:1.75. After 60 min, a paste-like material was recovered and directly subjected to carbonization at 900 °C under N_2 atmosphere (heating rate 1 °C min^{-1}, dwell time 1 h).

Activation. The OMC was ground in an agate mortar and activated with KOH using two routes: (i) impregnation with a 6 M KOH aqueous solution, and (ii) physical mixing with KOH pellets in an agate mortar. For materials activated by route (i), the OMC was added to the KOH aqueous solution and kept under stirring for 1 h, then, to remove the water, the dispersion was heated at 70 °C under vacuum until a slurry was obtained. Different initial amounts of solution were used to change the KOH/OMC weight ratio. Then, the impregnated OMC was subjected to heat treatment at 800 °C under N_2 atmosphere (flow rate 150 mL min^{-1}, heating rate 5 °C min^{-1}; dwell time 1 h and natural cooling). For materials activated by route (ii), the OMC was mixed with KOH in an agate mortar, using different KOH/OMC weight ratios, and subjected to the same heat treatment as for route (i). For materials activated by route (i), prior to the heat treatment, a drying step at 70 °C under vacuum was performed until a slurry was obtained. All the ACs were washed to remove residues from the activation process, mainly carbonates, with 1 M HCl aqueous solution, then water and finally dried at

105 °C. The materials were labeled OMC-*x*-*r* where "*x*" stands for the KOH-incorporation route, either *imp* or *pm* for routes (i) or (ii), respectively, and "*r*" stands for the KOH/carbon weight ratio ranging from 3 to 8.

The CO_2-activated OMC data from our previous study are presented for comparison [37]. Briefly, CO_2 activation was carried out at 900 °C for times ranging from 15 to 120 min. Herein, CO_2-activated samples are referred to as OMC-CO_2-*t*, where *t* stands for the activation time in minutes.

Morphological characterization. TEM images were acquired with a JEOL JEM – ARM 200F Cold FEG instrument operating at 200 kV and equipped with a spherical aberration probe corrector. For observation, low-power sonication was used to disperse the powdered samples in ethanol, and then a drop of the suspension was deposited on a carbon-coated copper grid (200 mesh) and allowed to dry in air before being placed in the equipment. In addition, a Bruker D8 ADVANCE X-ray diffractometer was used to perform small-angle X-ray diffraction (XRD) measurements. The corresponding device is equipped with an X-ray source with a Cu anode (operated at 40 kV and 40 mA), a graphite monochromator, and a scintillation detector. Data for the (100) bands were recorded, using silver behenate as reference for height correction.

Textural properties. N_2 and CO_2 adsorption isotherms (at -196 and 0 °C, respectively) were acquired using automatic adsorption devices, namely 3Flex and ASAP 2020 for N_2, and ASAP 2420 for CO_2 (Micromeritics). Secondary vacuum outgassing at 110 °C was carried out before adsorption analysis. Hysteresis loop scanning of the N_2 isotherms was performed using the following process: (i) adsorption was recorded until the relative pressure (p/p_0) reached a value of 1, then desorption was carried out until $p/p_0 = 0.2$; (ii) adsorption was again recorded until a relative pressure of less than 1; (iii) desorption was recorded until $p/p_0 \approx 0.3 – 0.4$; finally, steps (ii) and (iii) were repeated while gradually decreasing the maximum

value of p/p_0 reached during adsorption in step (ii). The BET area (A_{BET}, $m^2\ g^{-1}$) of the as-synthesized and activated OMCs was calculated using the Microactive® software (Micromeritics) and following the criteria suggested by the IUPAC [38]. The SAIEUS® software (Micromeritics) was used to apply the 2D non-local density functional theory for heterogeneous surface (2D-NLDFT HS) to the N_2 and CO_2 isotherms, allowing obtaining the pore size distributions (PSDs). From these data, textural properties such as surface area (S_{NLDFT}, $m^2\ g^{-1}$), total pore volume (V_{tot}, $cm^3\ g^{-1}$), ultramicropore volume ($V_{u\mu}$, $cm^3\ g^{-1}$, pore width, $w < 0.7$ nm), supermicropore volume ($V_{s\mu}$, $cm^3\ g^{-1}$, $0.7 < w < 2$ nm), and mesopore volume (V_{meso}, $cm^3\ g^{-1}$, $2 < w < 50$ nm) were calculated. In addition, the average pore width (w_{av}, nm) at different ranges was calculated by:

$$w_{av} = \frac{\sum_i \left(\frac{dV}{dw}\right)_i w_i}{\sum_i \left(\frac{dV}{dw}\right)_i} \quad (1)$$

Chemical composition. Elemental analysis (EA) was performed in a Vario EL Cube analyzer (Elementar) to measure the bulk contents of C, H, N, S, and O. Prior to measurements, the samples were dried at 105 °C to remove moisture, and then a small amount of material (~2 mg) was placed in the equipment to be burned in a furnace from which the gas is separated using trapping and chromatographic columns. A thermal conductivity detector quantifies the gases from which carbon, hydrogen, nitrogen and sulfur contents can be calculated. The oxygen content was measured separately in another column using a similar procedure.

An ESCAPlus OMICROM system was used to perform X-ray photoelectron spectroscopy (XPS) to study the surface chemistry of the materials. The device has an area of analysis of 1.75 × 2.75 mm, an Mg X-Ray source (1253.6 eV, operated at 15 kV and 15 mA), and was equipped with a hemispherical electron energy analyzer. Survey scans were carried out using a pass energy of 50 eV, and 20 eV were used for high-resolution scans. To obtain the atomic

content of each element and identify the different C and O functionalities, the CASA software was used to treat the C1s and O1s peaks of the XPS spectra.

Water affinity. The water affinity of KOH- and CO_2-activated OMCs was evaluated through water adsorption isotherms at 20 °C obtained with a 3Flex adsorption device (Micromeritics). Prior to the adsorption analysis, the samples were outgassed at 110 °C. An apparent water affinity constant was calculated from the slope of the isotherms in the low relative pressure range, $p/p_0 < 0.2$.

Electrochemical characterization. The studied carbon material was mixed with carbon black and PTFE in a weight ratio of 85:5:10 to prepare a paste from which disk-shaped electrodes (5 mm diameter) were cut. The carbon load (CL) of the electrodes was 9.1 ± 0.4 mg cm^{-2} and their thickness was 285 ± 14 µm, *i.e.*, similar characteristics to those used in commercial devices. The electrodes were impregnated with 1 M H_2SO_4 used as an aqueous electrolyte and placed in a two-electrode cell with gold current collectors for testing. The SC cells were assembled using two electrodes of the same material and similar mass, separated by a porous glass fiber mat, and the electrochemical characterization was carried out using a VSP-300 electrochemical workstation (Bio-logic). Cyclic voltammetry (CV) curves were obtained within a potential window of 1 V and the specific cell capacitance (C_{cell}, F g^{-1}) was calculated using the following equation:

$$C_{cell} = \frac{\oint I_{meas} dV}{s \Delta V m} \quad (2)$$

where I_{meas} represents the measured current in A, s the scan rate in mV s^{-1}, ΔV the potential window in V, and m the mass of active material in the two electrodes in g. Galvanostatic charge-discharge (GCD) curves, also performed using a potential window of 1 V, were used to calculate C_{cell} from the equation:

$$C_{cell} = \frac{I_{ap}}{(dV/dt)m} \quad (3)$$

where I_{ap} represents the applied current in A, based on the mass of active material in one electrode in g, m is again the mass of active material in the two electrodes in g, and dV/dt is the slope of the discharge curve in V s^{-1}, determined using the upper half of the curve and after removing the potential drop (iR) [39,40]. Using the values of C_{cell} obtained from the GCD tests, the specific energy (E, Wh kg^{-1}) and power (P, W kg^{-1}) were calculated through:

$$E = \frac{1}{7.2} C_{cell}(V_1^2 - V_2^2) \quad (4)$$

$$P = 3600 \frac{E}{\Delta t_{12}} \quad (5)$$

where $V_1 = \Delta V - iR$ and $V_2 = 0$ in V, and Δt_{12} is the time required for complete discharge of the SC in s. The frequency response of the materials was evaluated by means of electrochemical impedance spectroscopy (EIS) measurements performed at open-circuit voltage using a sinusoidal signal with an amplitude of 10 mV and a frequency ranging from 10 mHz to 100 kHz. The EIS measurements provided the complex impedance of the system Z, whose real and imaginary parts (Z_r and Z_i, respectively, both in Ω) were used to obtain the Nyquist plots, and from which the real part of the complex capacitance (C_r, F) was calculated by:

$$C_r = \frac{-Z_i}{2\pi f |Z|^2} \quad (6)$$

where $|Z|$ is the modulus of the complex impedance in Ω, Z_i is the imaginary part of the complex impedance in Ω, and f is the frequency of the sinusoidal signal in Hz.

3. Results and discussion

3.1. Morphology and textural properties

Figure 1 shows TEM images of the as-synthesized and activated OMCs, where it is possible to observe their 2D hexagonal geometry before (Figure 1a and 1d) and after activation (Figure 1b, 1c, 1e, and 1f). These images show that the activated OMCs retain their ordered structure regardless of the KOH-incorporation route and even when high KOH/carbon mass ratios were used, see Figure 1b and 1e for the impregnation route (*imp*) and Figure 1c and 1f for the physical mixing route (*pm*). Small-angle XRD patterns, shown in Figure 1g and 1h, exhibit the characteristic (100) band, confirming the presence of the ordered structure and evidencing that the mesostructure was preserved after activation, independent of the KOH-incorporation route. Small-angle XRD results also revealed that the mesostructure is better preserved after KOH-activation than after CO_2-activation. Indeed, a lesser deformation of the (100) band is observed with increasing *r* than with increasing activation time (*t*) under CO_2 atmosphere, see the OMC-CO_2-*t* series of Figure 1i. In addition, it should be noted that the position of the (100) band shifts in opposite directions for KOH- and CO_2- activated materials, which could be explained by the different mechanisms of activation. KOH activation creates microporosity through the intercalation of metallic K into the carbon framework [41]; this increases the thickness of the pore walls and produces an overall widening of the unit cell. This therefore explains the slight shift of the (100) band position to lower values of 2θ, which are associated to larger d_{100} interplanar spacing as shown in Figure S1 of the Supplementary Information (SI). On the contrary, CO_2 activation develops porosity through partial gasification of the material, which causes weakening of the mesoporous structure and its partial collapse. Such collapse would lead to a reduction in the d_{100} interplanar spacing (see again Figure S1), thus explaining the shift to higher values of 2θ. This behavior is in agreement with the previous remark of a better preservation of the mesoporous structure by KOH activation.

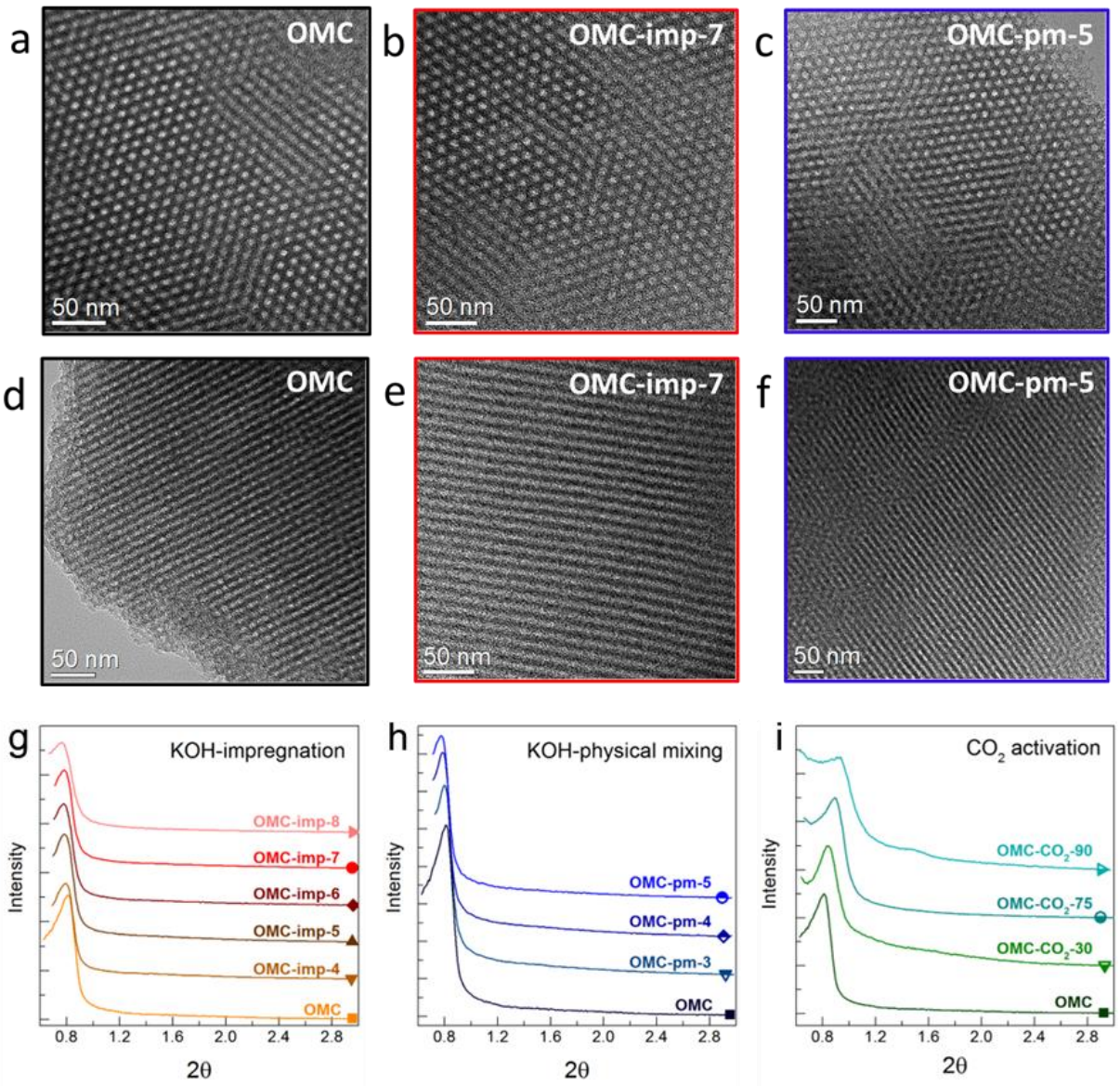

Figure 1. TEM images of OMCs before (a, d) and after activation by: (b, e) impregnation and (c, f) physical mixing KOH-incorporation routes. Small-angle XRD measurements for: (g) OMC-*imp*-*r*, (h) OMC-*pm*-*r*, and (i) OMC-CO_2-*t* series of activated materials (TEM images of OMC material and data for the OMC-CO_2-*t* series are from Castro-Gutiérrez et al. (2019) [37]).

Figure 2a and 2b show the N_2 adsorption-desorption isotherms for the two series of activated OMCs in this study. In all cases, the isotherms are a combination of types I and IV [38], which are commonly observed for micro-mesoporous materials. The increasing gas uptake at low relative pressures ($p/p_0 < 0.2$) indicates a development of microporosity with increasing *r*,

which is also observed on the pore size distribution (PSDs, Figure 2d and 2e). It is also worth noting from the PSDs that KOH activation develops and widens the microporosity, while CO_2 activation appears to widen predominantly the existing microporosity (see Figure 2f). At higher relative pressures (p/p_0 > 0.4), the characteristic hysteresis loops of the OMC materials were also observed, *i.e.*, H2a hysteresis loops [38]. Note also that the shape of the hysteresis loops remains almost unchanged with increasing *r*, unlike the loops obtained from the OMC-CO_2-*t* series in Figure 2c. This indicates that the mesoporous structure is better preserved by KOH-activation, in agreement with the small-angle XRD results presented above (Figure 1g-i). Indeed, in the mesopore range, the PSDs revealed that the narrow peak centered at ~5 nm widens and increases in size after KOH activation. In contrast, for CO_2-activated materials, the same peak notoriously widens and shifts its position to a narrower pore width due to a larger development of narrow mesopores, as shown in Figure 2g-i and Figure S2.

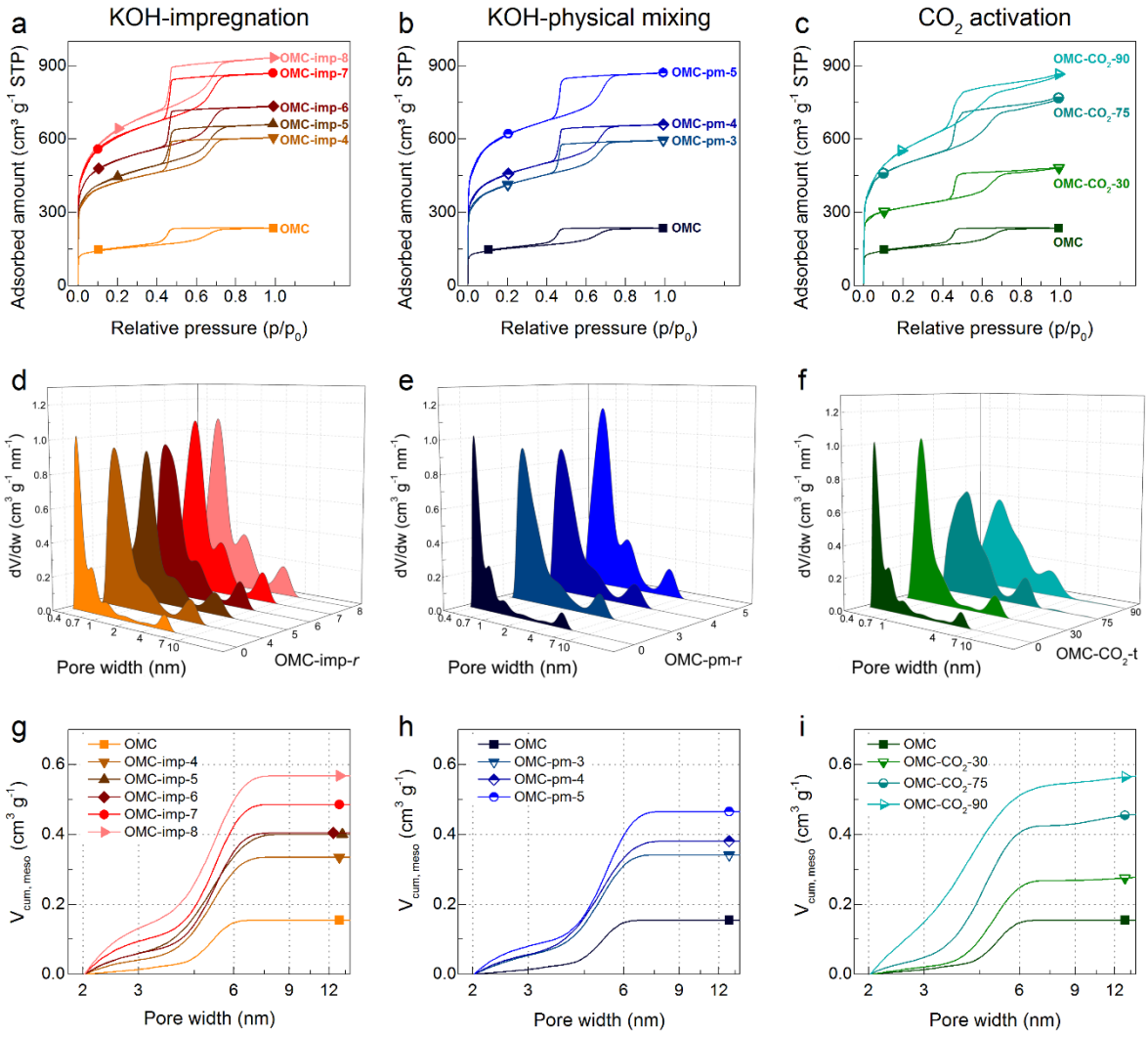

Figure 2. (a-c) Nitrogen adsorption-desorption isotherms, (d-f) differential PSDs, and (g-i) cumulative PSDs in the mesopore range for the (a, d, g) OMC-*imp-r*, (b, e, h) OMC-*pm-r*, and (c, f, i) OMC-CO_2-*t* series of materials (Data for the OMC-CO_2-*t* series are from Castro-Gutiérrez et al. (2019) [37]).

The calculated textural parameters of the activated materials, such as surface area (S_{NLDFT}), total pore volume (V_{tot}), and pore volume at different ranges of pore width are reported in Table S1 of the SI. For comparison, the area obtained by applying the BET method to N_2 isotherms (A_{BET}) is also reported in Table S1. However, due to the known uncertainties of the BET method when there is a high presence of micropores [38], in-depth analysis of the textural properties and their relationship to water affinity, surface chemistry, and electrochemical behavior was performed using values of S_{NLDFT}.

Figure 3a shows that S_{NLDFT} increases with *r* for both series of activated OMCs and reaches values close to 2000 $m^2\ g^{-1}$. It should also be noted that the *pm* KOH-incorporation route seems to be more efficient since it requires lower amounts of activating agent, *i.e.*, lower values of *r*, to achieve similar S_{NLDFT} values as the *imp* route. In addition, the *pm* route exhibits higher values of burn-off (*BO*) than the *imp* route (see Table S1). This difference in activation efficiency between the two KOH-incorporation routes could be due to a low affinity of the material for water, discussed in more detail in Section 3.3. Besides, a previous study showed that access to mesopores in tannin-derived OMCs is limited since mesopores are mainly accessible through narrow micropores (~0.5 nm wide) [42]. Thus, the combination of hydrophobicity and low pore connectivity could prevent the access of KOH aqueous solution to the inner porosity of the carbon particles, thereby delaying the activation process. In addition, some studies on KOH activation of coals with a high presence of micropores have reported inhibition of activation due to the presence of water [43,44]. It has been hypothesized that, as the temperature increases during the drying step, KOH is drawn to the outside of the material by water. Therefore, this causes the reactions to occur mainly at the periphery of carbon particle [44], and results in the delayed development of porosity in OMC-*imp-r* series materials compared to OMC-*pm-r* series materials.

Despite the differences in activation efficiency, Figure 3b shows that the ultramicro-, supermicro- and mesoporous volumes ($V_{u\mu}$, $V_{s\mu}$, and V_{meso}, respectively) of the materials all follow the same trend when plotted as a function of S_{NLDFT}, regardless of the activation route. Specifically, $V_{u\mu}$ increases slightly from ~0.15 $cm^3\ g^{-1}$ to a maximum of ~0.2 $cm^3\ g^{-1}$ at ~1500 $m^2\ g^{-1}$ and then it decreases slightly, whereas $V_{s\mu}$ increases with S_{NLDFT} from ~0.1 to 0.6 $cm^3\ g^{-1}$. The evolution of $V_{u\mu}$ and $V_{s\mu}$ is consistent with previous studies reporting that KOH activation at temperatures above 700 °C leads to development and enlargement of the existing microporosity. This is also reflected by the increase in the average width of ultramicro- and

supermicropores ($w_{av,u\mu}$ and $w_{av,s\mu}$, respectively) shown in Figure S3. The mesopore volume (V_{meso}) increases with S_{NLDFT} from ~0.2 to 0.6 $cm^3\ g^{-1}$, however, the average mesopore width ($w_{av,meso}$) decreases with activation. This decrease in $w_{av,meso}$ can be explained by the fact that KOH activation develops mainly pores with widths smaller than 3 nm (see Figure S2), thus shifting the average width to lower values even if V_{meso} increases. In contrast, a different behavior is observed for CO_2-activated materials, see Figure S3 and S4: $w_{av,s\mu}$ decreases drastically for low activation times due to an opening of blocked micropores, then activation widens these pores thus increasing the average pore width. Through CO_2 activation, the surface area reaches lower values than those obtained by KOH activation with a maximum at ~1600 $m^2\ g^{-1}$ after 75 min of activation. Longer activation times result in high *BO* causing pore merging and eventual loss of porosity due to the collapse of the pore structure, as $V_{s\mu}$ and V_{meso} both decrease drastically for 120 min of activation (*BO* = 94 %) [37]. Regarding the mesopores, $w_{av,meso}$ increases slightly with activation due to the widening of the mesoporous channels, *i.e.*, those associated with the peak at ~5 nm of the PSD, and the pores connecting those channels (w < 5 nm). After 90 min of activation, $w_{av,meso}$ drops sharply as the contribution of narrower pores becomes more significant (see Figure S2 and S3).

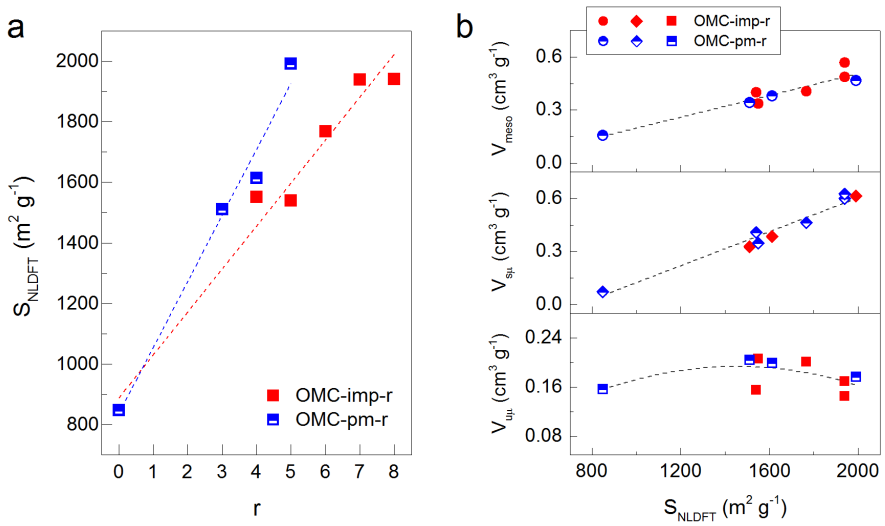

Figure 3. (a) Surface area calculated using the 2D-NLDFT HS (S_{NLDFT}) as a function of the KOH/carbon weight ratio (r). (b) Pore volume as a function of S_{NLDFT} for mesopores (V_{meso}), supermicropores ($V_{s\mu}$) and ultramicropores ($V_{u\mu}$).

Scanning of the hysteresis loops of N_2 adsorption-desorption isotherms was performed to further characterize the materials. Partial filling of the pore network produces secondary desorption branches and by studying their behavior it is possible to obtain information about the pore network connectivity of a material [45,46]. Examples of scanned hysteresis for one material from each series of activated carbons studied (OMC-*imp*-*r*, OMC-*pm*-*r*, and OMC-CO_2-*t*) are shown in Figure S5. In a previous study by our group, it was shown that it is possible to evaluate whether access to mesopores is restricted by observing the changes in the shape of these secondary desorption branches [47]. Figure S5a and S5b show that the analyzed materials exhibit straight secondary desorption branches regardless of the KOH-incorporation route, as previously observed for CO_2-activated materials (Figure S5c).

In Figure 4, the slope of the desorption branches is plotted as a function of their starting point $(p/p_0)_{des}$. In Figure 4a and 4b, it can be observed that for KOH-activated materials, the desorption rate, *i.e.*, the slope, is almost constant for $(p/p_0)_{des} > 0.7$. This delayed desorption from the wider mesopores indicates that these mesopores are connected through narrow pores less than 5 nm wide [45,48]. For $(p/p_0)_{des} < 0.7$, the desorption rate increases with $(p/p_0)_{des}$, suggesting hindered desorption from the narrow mesopores. Note that the same behavior is observed for the as-synthesized and activated materials. Moreover, the desorption rate at lower values of $(p/p_0)_{des}$ is more pronounced for the activated OMCs, suggesting that there are no significant changes in terms of pore network connectivity after activation by any of the KOH incorporation routes. On the contrary, Figure 4c shows the changes in the desorption rate for $(p/p_0)_{des} < 0.7$ for the CO_2-activated materials, which suggest an improvement to some extent in the pore network connectivity [47].

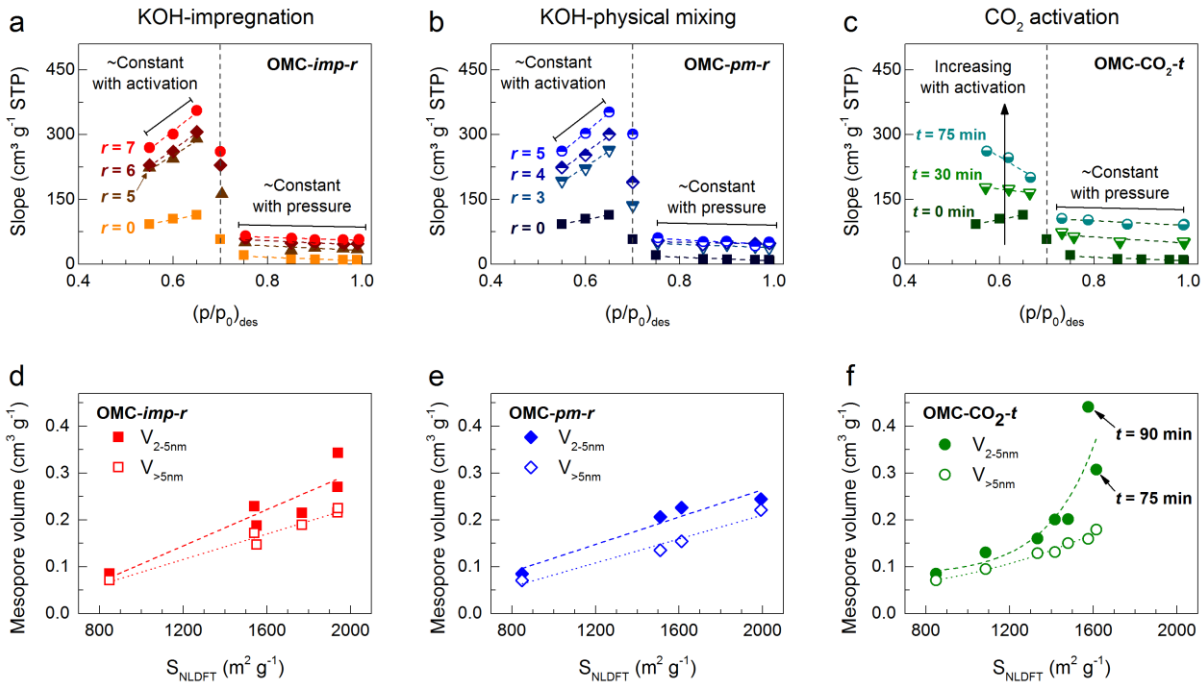

Figure 4. (a-c) Slope of scanning desorption branches as a function of their starting point, $(p/p_0)_{des}$, and (d-e) contribution to the mesoporous volume of pores with widths below and above 5 nm ($V_{2–5nm}$ and $V_{>5nm}$, respectively) for the materials: (a, d) OMC-*imp-r*, (b, e) OMC-*pm-r*, and (c, f) OMC-CO_2-*t* (Data for the OMC-CO_2-*t* series are from Castro-Gutiérrez et al. (2021) [47]).

Analysis of the desorption rates indicates that although KOH activation results in the development of narrow mesopores between 2 and 5 nm in width (see Figure 4d and 4e), a large portion of these pores most likely originate from micropores formed by the intercalation of metallic K into the carbon framework [41]. In this case, these newly formed pores would not necessarily be connected to each other, which explains the lack of improved pore network connectivity to access the wider channels in the mesoporous structure. In contrast, textural characterization indicates that CO_2 activation primarily unblocks and expands the existing porosity, which is reflected by the fact that $V_{u\mu}$ decreases with activation while $V_{s\mu}$ increases, *i.e.*, no new porosity is created. Nonetheless, CO_2 activation effectively increases the volume of the mesopores due to the widening of narrow mesopores (see Figure 4f) and improves the connectivity of the pores due to pore merging, facilitating the desorption accordingly with the changes in desorption rates observed in Figure 4c.

3.2. Chemical characterization

The EA results reported in Table S2 show that oxygen is the main heteroatom present in the carbon structure and decreases with activation, as shown in Figure 5a. On the other side, Figure 5b shows the O content at the surface, in wt.%, measured by XPS and Figure 5c shows the O content at the surface divided by S_{NLDFT} (O/S_{NLDFT}, µmol m^{-2}), which could be considered as O concentration at the surface; all values are also reported in Table S2. In general, the O content at the surface is slightly higher than that in the bulk. The contribution of the different surface functional groups to the O content is given in Table S3 for all materials. In all cases, due to the nature of the precursor, the major contribution to the surface O moieties, ~75 – 85 %, comes from phenolic groups (OII), followed by quinone- and carbonyl-type groups (OI) with contributions in the range of 10 – 20 %, the rest coming from carboxylic groups (OIII) and, in some cases, from chemisorbed oxygen or water (OIV). Furthermore, it can be observed in Figure 5c that KOH activation of OMC materials removes oxygen from the carbon surface, as the O content and O/S_{NLDFT} decrease with increasing S_{NLDFT}. On the other hand, O/S_{NLDFT} decreases for CO_2-activated materials with S_{NLDFT} up to ~1400 m^2 g^{-1}, but increases again for materials with higher S_{NLDFT} (~1600 m^2 g^{-1}), see Figure 5d. It should be noted that for materials with similar S_{NLDFT}, CO_2 activation produces materials with higher O/S_{NLDFT} than KOH-activation, which affects the water affinity and electrochemical performance of the materials, as detailed below.

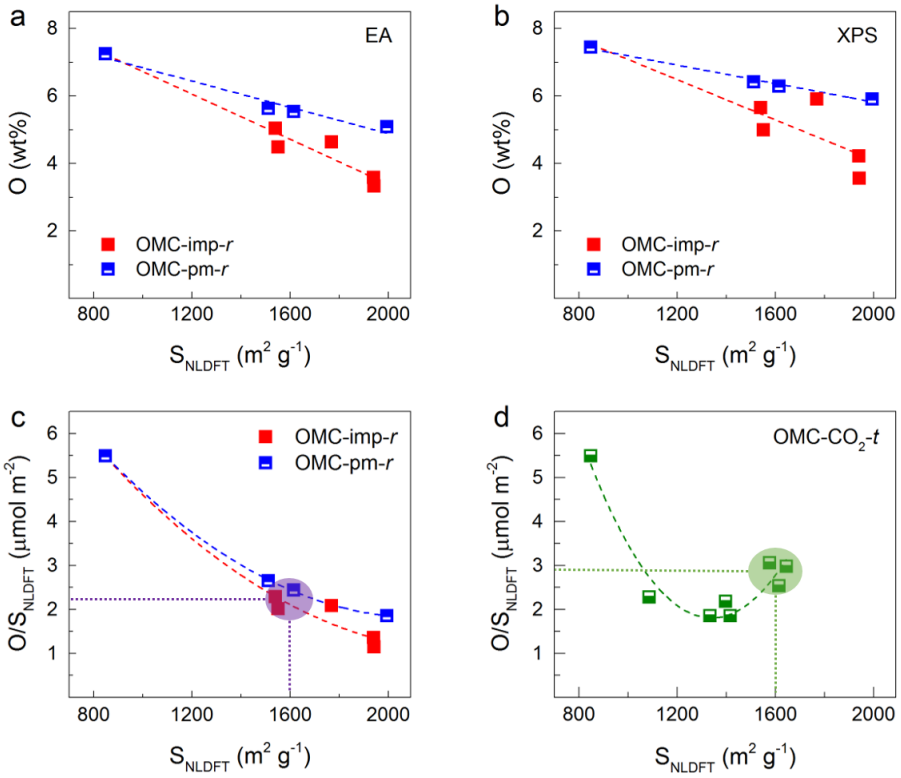

Figure 5. (a) Bulk and (b) surface oxygen content, measured by elemental analysis (EA) and X-ray photoelectron spectroscopy (XPS), respectively, for OMC-*imp-r* and OMC-*pm-r* series. (c, d) Surface oxygen concentration (O/S_{NLDFT}), calculated from XPS measurements, as a function of surface area (S_{NLDFT}) of OMC-*imp-r*, OMC-*pm-r*, and OMC-CO_2-*t* materials.

3.3. Water affinity

Water adsorption isotherms at 20 °C of pristine and activated OMCs were obtained to evaluate their affinity for water. Although this is an important parameter, since activated OMCs are intended to be used as electrodes for SCs in aqueous electrolytes, water affinity is not normally evaluated in relation to such an application.

Figure 6a shows representative examples of the acquired water adsorption isotherms of the materials in this study, specifically OMC, OMC-*pm*-3, and OMC-CO_2-30. The water isotherms of an oxidized carbon molecular sieve (CMS-ox) [23] and a commercial zeolite (NaY) [24] are also shown for comparison. As mentioned previously, water adsorption at low relative pressure is primarily governed by the presence of functional groups and can be used

to estimate the water affinity – hydrophilicity or hydrophobicity – of carbon materials [21,24–26]. From Figure 6a, it is possible to observe that, unlike the case of commercial NaY zeolite considered as a hydrophilic material and having a high water uptake in the $p/p_0 < 0.2$ region, OMC exhibits a hydrophobic behavior. The hydrophobicity of the OMC would explain the observation of different activation efficiencies of KOH-incorporation routes, as detailed in Section 3.1. CMS-ox shows an intermediate behavior between the hydrophilic NaY zeolite and the hydrophobic OMC, due to the introduction of oxygen functionalities on the carbon surface by oxidation [23]. From the changes in the water adsorption behavior at low p/p_0, it can be noted that CO_2 activation appears to improve the water affinity of the OMC material while KOH activation renders the material highly hydrophobic. The effect of the activation process on the water affinity of the resultant OMC materials is discussed in more detail below.

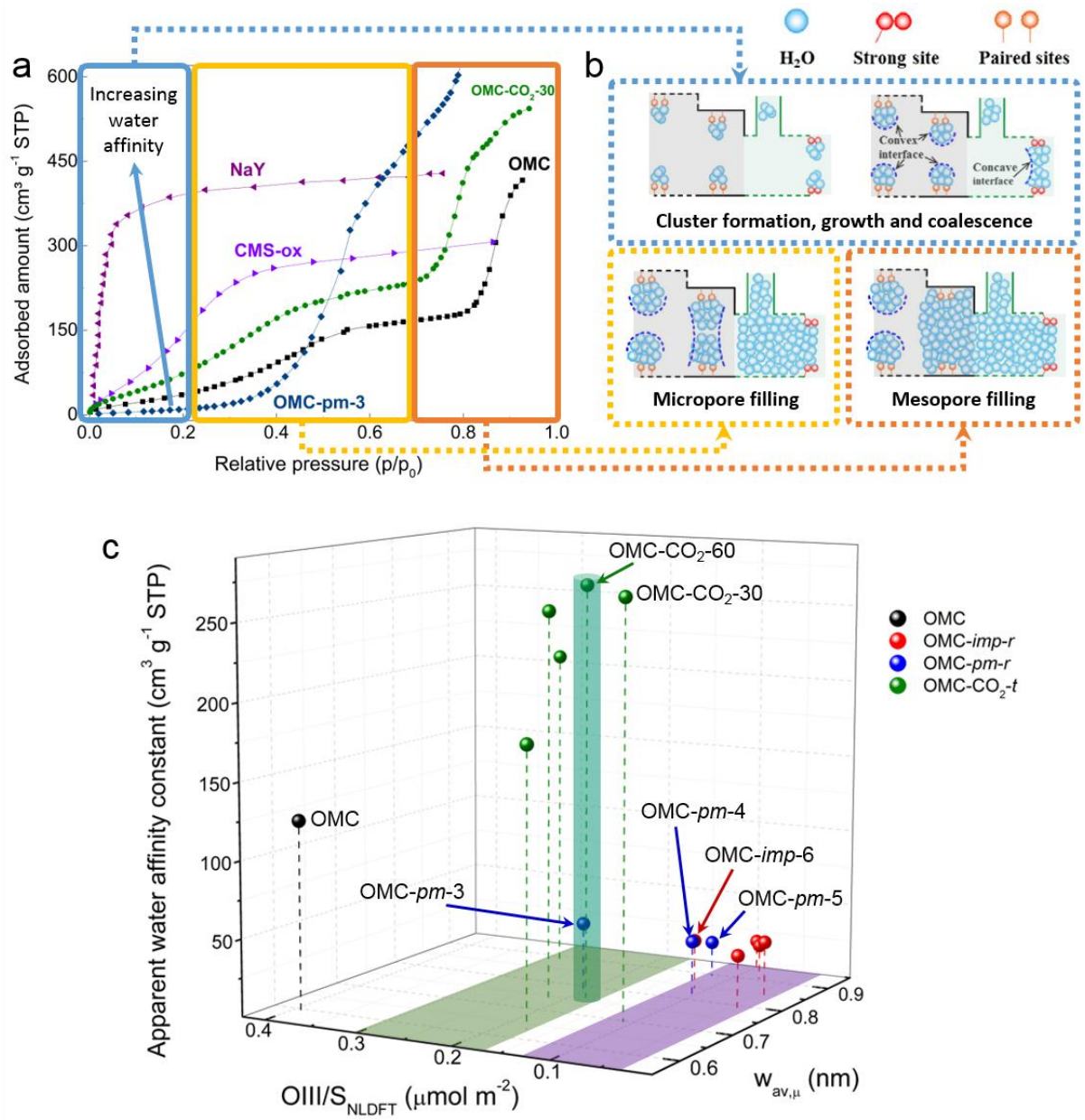

Figure 6. (a) Water adsorption isotherms at 20 °C of OMC, OMC-*pm*-3, and OMC-CO_2-30 compared with those of a carbon molecular sieve oxidized using nitric acid (CMS-ox) [23] and the commercial zeolite NaY (at 30 °C) [24]. (b) The different stages of water adsorption are shown (adapted from Liu, L. et al., *Adv. Colloid Interface Sci.* (2017), with permission from Elsevier [21]). (c) Apparent affinity constant calculated from water adsorption isotherms at low relative pressure as a function of the surface carboxylic group concentration ($OIII/S_{NLDFT}$) and average micropore width ($w_{av,\mu}$).

It is generally accepted that the complex behavior of water adsorption in carbon materials, schematically shown in Figure 6b, is due to the combination of: (i) the interaction of water with active sites, predominantly carboxylic groups (cluster formation); (ii) the interaction of water with clusters acting as nucleation sites (cluster growth and coalescence); and (iii) the

water-carbon interaction related to the pore size (micropore and mesopore filling) [21,22,26,49–51]. In water adsorption isotherms, the adsorption behavior at different p/p_0 ranges can be associated to a greater or lesser extent with these interactions, as shown in Figure 6c. In order to relate the water affinity and the physicochemical properties of the activated OMCs, by KOH or CO_2 activation, an apparent affinity constant was calculated for each material. This constant was defined as the slope of the linear part of the adsorption isotherms in the low-relative pressure region ($p/p_0 < 0.2$), considered as the region where the (i-iii) interactions are strongest and can be related to the water affinity of the materials [21]. Figure 6c shows the calculated values of the apparent affinity constant as a function of the surface concentration of carboxylic groups ($OIII/S_{NLDFT}$), associated with interactions (i) and (ii), and as a function of the average micropore width ($w_{av,\mu}$) accounting for interaction (iii).

From Figure 6c, several cases should be noted, firstly the fact that CO_2-activated materials have, in general, higher values of $OIII/S_{NLDFT}$ than KOH-activated materials. Since interaction (i) is strongest in the low-relative pressure regime, this higher concentration of active oxygen sites directly increases the water affinity of the CO_2-activated materials. This statement seems to be in contradiction with the case of the OMC material, which has a lower affinity for water than the CO_2-activated OMCs although it has the highest $OIII/S_{NLDFT}$ value among all samples. However, it has been reported that water adsorption might be inhibited in pores with widths smaller than 0.6 nm because a hydrogen-bonded tetrahedral water cluster, typically 0.7 nm high, would have to rearrange itself to fit inside such narrow pores [21,22,51]. This rearranging would hamper the adsorption process, thus explaining the lower water affinity of OMC. On the other hand, other activated OMCs with similar $OIII/S_{NLDFT}$ values but different $w_{av,\mu}$ are also plotted, specifically OMC-CO_2-30, OMC-*imp*-6, OMC-*pm*-4, and OMC-*pm*-5. Simulation studies of water adsorption in carbon slit-shaped nanopores have suggested that the water-carbon interaction (iii) in the pores changes drastically in the $w_{av,\mu}$ range of 0.6 – 1.0

nm, increasing as $w_{av,\mu}$ decreases and reaching a maximum at $w_{av,\mu}$ = 0.7 nm [51]. The results shown in Figure 6b are in agreement with these simulation studies. Among the samples considered, OMC-CO_2-30 exhibits a considerably higher water affinity, most likely due to a stronger water-carbon interaction in its narrow pores ($w_{av,\mu}$ = 0.7 nm) than that of KOH-activated counterparts with similar $OIII/S_{NLDFT}$ but wider pores (0.8 < $w_{av,\mu}$ < 0.9 nm). Finally, another interesting case is presented for the OMC-CO_2-60 and OMC-*pm*-3 samples, which have almost the same $OIII/S_{NLDFT}$ and $w_{av,\mu}$ (~0.2 µmol m^{-2} and ~0.8 nm, respectively) but the water affinity of OMC-CO_2-60 is about 6 times higher than that of OMC-*pm*-3. This difference in water affinity could be due to heterogeneities in surface chemistry, such as the presence of different types of functional groups or the relative position of active sites on the same or opposite pore walls. It has been reported that these heterogeneities play a significant role in the mechanisms of water adsorption in carbon materials [22,52,53]. However, it has been shown here that KOH-activated materials exhibit low pore connectivity (see Figure 4a,b). Thus, in addition to surface heterogeneity factors, it is likely that water adsorption in OMC-*pm*-3 is hindered by difficult access of water molecules to the active sites, which accounts for its considerably lower water affinity than OMC-CO_2-60. In this sense, in addition to the average pore size, the better pore connectivity of OMC-CO_2-30 compared to that of KOH-activated materials could also be a contributing factor to the increase in its affinity for water described above.

3.4. Electrochemical characterization

Electrochemical tests were performed in 1 M H_2SO_4 aqueous solution using three KOH-activated OMCs as electrode materials. The samples OMC-*imp*-7 and OMC-*pm*-5 were chosen to study the effect of the KOH-incorporation route due to their comparable high S_{NLDFT}, ~2000 m^2 g^{-1}. The third selected sample, OMC-*pm*-4, with a similar S_{NLDFT} to that of OMC-

CO_2-75, ~1600 m^2g^{-1}, was tested to analyze the effect of the activation process by direct comparison with the electrochemical performance of CO_2-activated OMC, which has been previously tested as an electrode material for supercapacitors with satisfactory results in an aqueous electrolyte (1 M H_2SO_4) [37].

3.4.1. Effect of the KOH-incorporation route

Cyclic voltammetry (CV) tests using OMC-*imp*-7 and OMC-*pm*-5 materials were performed at scan rates from 5 to 500 mV s^{-1}. Figure 7a and 7b show examples of the CV curves obtained. Their near-rectangular shape indicates SC behavior; however, note that the curves have small humps suggesting the occurrence of Faradaic reactions at low scan rates. The redox humps are less pronounced for OMC-*imp*-7, which has a lower O/S_{NLDFT} than OMC-*pm*-5. As the scan rate increases, Faradaic reactions are progressively reduced and the redox humps on the CV curves eventually fade (see again Figure 7a and 7b). Figure 7c shows that at a low scan rate of 5 mV s^{-1}, OMC-*pm*-5 and OMC-*imp*-7 achieved a high specific cell capacitance (C_{cell}) of 50 F g^{-1} due to their high S_{NLDFT}. As the scan rate increases, C_{cell} decreases drastically for both materials and it can be observed that the capacitance retention (C_{ret}) is 5% higher for OMC-*pm*-5.

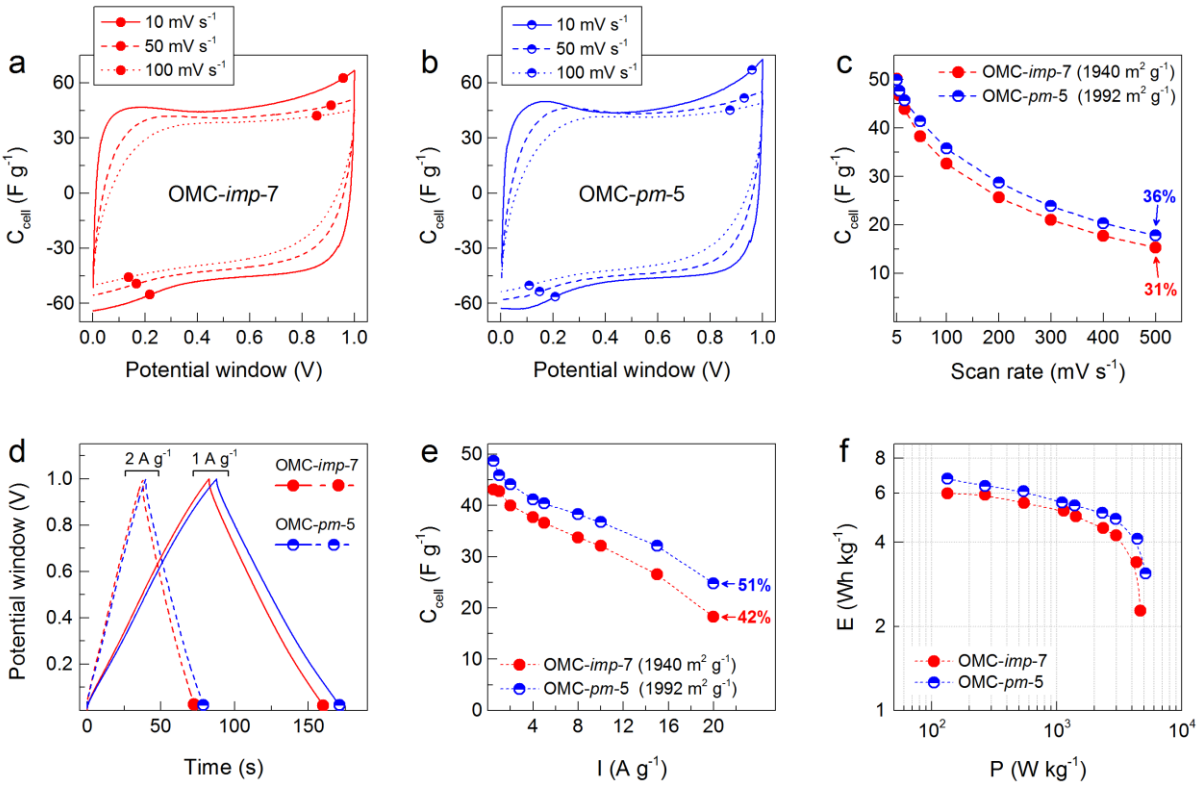

Figure 7. Electrochemical performance of KOH-activated OMCs by the impregnation and physical mixing incorporation routes, OMC-*imp*-7 and OMC-*pm*-5, respectively. CV curves at different scan rates for (a) OMC-*imp*-7 and (b) OMC-*pm*-5; (c) specific cell capacitance (C_{cell}) as a function of scan rate; (d) charge-discharge curves at 1 and 2 A g^{-1}; (e) C_{cell} as a function of specific applied current (I); the capacitance retention at 500 mV s^{-1} for CV curves and 20 A g^{-1} for GCD, and S_{NLDFT} values for each material are also indicated; (f) Ragone-like plot.

Galvanostatic charge-discharge (GCD) tests were performed by varying the specific applied current (I) from 0.5 A g^{-1} to 20 A g^{-1}; Figure 7d shows examples of curves obtained at 1 and 2 A g^{-1}. The curves are triangular, indicating SC behavior. C_{cell} was calculated from the discharge curve and is shown in Figure 7e as a function of I, and OMC-*pm*-5 consistently outperformed OMC-*imp*-7 in agreement with the CV results. At 0.5 A g^{-1}, C_{cell} reached maximum values of 49 F g^{-1} for OMC-*pm*-5 and 43 F g^{-1} for OMC-*imp*-7. As I increased, the capacitance decreased, exhibiting capacitance retentions of 51 and 42 % for OMC-*pm*-5 and OMC-*imp*-7, respectively (see Figure 7e again). Nevertheless, these C_{ret} values were higher than those obtained from the CV experiments, indicating that these materials have less resistance to electron mobility than to ion mobility, which are the respective charging

mechanisms of the GCD and CV tests [54]. This restricted ion mobility can be related to the low affinity of these materials for water (see Figure 6c), as diffusion of solvated ions through a hydrophobic surface would indeed be hindered. The better performance of OMC-*pm*-5 compared to OMC-*imp*-7 could be explained by considering that, as described in the previous sections, the *imp* route could develop porosity mainly on the outer surface of the carbon particles due to the restricted access to the pores and the low water affinity of OMC. Thus, the *imp* route would lead to the formation of more pores that are not connected to the internal porosity, resulting hindered ion diffusion in OMC-*imp*-7 compared to the OMC-*pm*-5 material obtained by the *pm* route.

Figure 7f shows the Ragone-like plot with the specific energy and power values (*E* and *P*, respectively) of the SC cells calculated from the GCD curves. At the lowest specific applied current of 0.5 A g^{-1}, the OMC-*pm*-5 cell has a maximum storage capacity of 7 Wh kg^{-1} with a power of 133 W kg^{-1}, while the OMC-*imp*-7 cell exhibits a maximum storage capacity of 6 Wh kg^{-1} at the same power. These values of *E* and *P* are within the range reported for similar materials and testing conditions in H_2SO_4, as shown in Table S4 [18,37,47,55–68].

3.4.2. Effect of the activation process

KOH activation was used in this study with the aim of producing materials with larger surface areas and more developed porosity than those obtained by CO_2 activation, in order to further improve the electrochemical performance of tannin-derived materials. Indeed, at low charging rates, the C_{cell} and *E* values achieved for OMC-*pm*-5 and OMC-*imp*-7 are higher than those obtained under the same conditions with CO_2-activated materials [37], due to their larger surface area. However, when comparing materials of similar surface area obtained by CO_2 or KOH activation, a more complex behavior is observed. This comparison shows that CO_2 is a

better choice of activating agent from the point of view of SC performance, environment and economy, as discussed below.

Figure 8a shows C_{cell} as a function of I during GCD tests for OMC-*pm*-4 and OMC-CO_2-75 samples, with S_{NLDFT} of 1613 and 1614 $m^2\ g^{-1}$, respectively. Note that for the OMC-*pm*-4 sample, C_{cell} reaches a high value of 49 $F\ g^{-1}$ at 0.5 $A\ g^{-1}$, the same as that achieved by OMC-*pm*-5 with a higher surface area (1992 $m^2\ g^{-1}$). Close inspection of the GCD curves at 0.5 and 1 $A\ g^{-1}$ revealed a Coulombic efficiency ($CE = t_{discharge}/t_{charge}$) greater than 1 for OMC-*pm*-4, see Figure S6. A CE > 1 is a sign of electrolyte decomposition, which could be promoted, especially at low charging rates, by the presence of O surface functionalities. Electrolyte decomposition produces excess charge that delays SC discharge, resulting in an apparent increase in capacitance, a behavior similar to that observed in Li-ion batteries due to Li accumulation in the overhand region [69]. For $I > 1\ A\ g^{-1}$, OMC-*pm*-4 exhibits $CE < 1$ and triangular-shaped GCD curves indicating SC behavior (Figure S6). For higher I, the capacitance values for the OMC-*pm*-4 material decrease significantly, as observed for OMC-*pm*-5 and OMC-*imp*-7 in Section 3.4.1, again suggesting that the surface is not easily accessible, thus preventing the formation of the EDL. In contrast, for the OMC-CO_2-75, a $CE \leq 1$ was always observed, even at the lowest I, and pseudocapacitance contributions occur only at low charging rates, $I < 1\ A\ g^{-1}$. For higher values of I, the capacitance remains nearly constant up to a current of 20 $A\ g^{-1}$, indicating that energy is stored by the EDL mechanism even at low charging rates. Furthermore, it was shown for OMC-CO_2-75 that, up to 80 $A\ g^{-1}$, C_{ret} still remains at 74 % (considering C_{cell} at 0.5 $A\ g^{-1}$ as the maximum) [37], while for the KOH-activated materials, C_{ret} is already below 20 % at 40 $A\ g^{-1}$, as shown in Figure S7. Besides, it was also found that the CO_2-activated material exhibited better long-term stability than the KOH-activated materials, see Figure S8. OMC-CO_2-75 exhibited a C_{ret} of 95 % after 10 000 continuous GCD cycles at 5 Ag^{-1} and 33 % potential loss after 24 h during self-

discharge measurements, while OMC-*imp*-7 and OMC-*pm*-5 exhibited ~87 % of C_{ret} after continuous cycling and a 44 % potential loss during self-discharge tests.

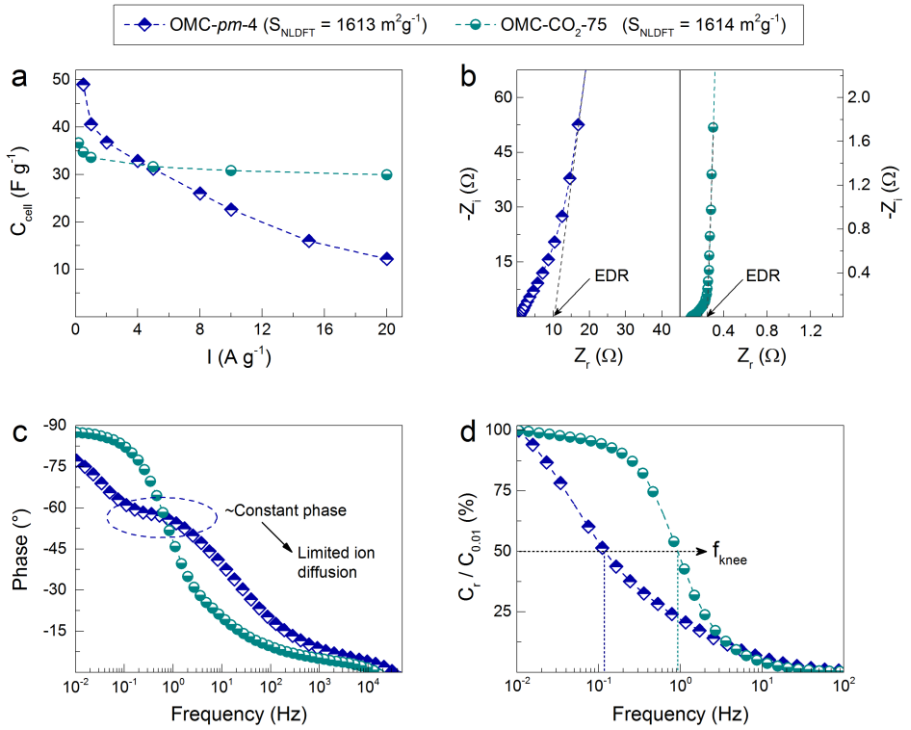

Figure 8. Comparison of electrochemical performance of two selected KOH- and CO_2-activated materials, OMC-*pm*-4 and OMC-CO_2-75, respectively: (a) Specific cell capacitance (C_{cell}) versus specific applied current (I); (b) Nyquist and (c) Bode plots; and (d) frequency response of the real part of the complex capacitance (C_r) normalized by the capacitance value at 0.01 Hz ($C_{0.01}$).

Electrochemical impedance spectroscopy (EIS) tests were performed to study the resistive behavior of the materials. Figure 8b and 8c show the Nyquist and Bode plots obtained from the EIS tests. It can be seen that the equivalent distributed resistance (EDR) is an order of magnitude higher for OMC-*pm*-4 than for OMC-CO_2-75 (Figure 8b). In addition, from the Nyquist plots, the intersection of the curves with the Z_r axis at high frequencies is between 0.1 and 0.3 Ω, which is consistent with the small *iR* drops found in the GCD measurements. Thus, EIS tests revealed that the most important contribution to the EDR of OMC-*pm*-4 comes from limited ion diffusion. The latter appears as a straight line at medium frequencies (MF,

between ~10^{-1} to ~10^{1} Hz) in the Nyquist plot and as a region of nearly constant phase in the Bode plot [70]. Ion diffusion for OMC-CO_2-75, in contrast, is not hindered because the straight line at MF in the Nyquist plot is very short (~0.1 Ω long), and there is no constant phase region visible in the Bode plot.

Furthermore, from the EIS measurements, the "knee" frequency, f_{knee}, which determines the point at which the electrolyte has achieved full access to the electrode surface, can be identified by analyzing the frequency response of the real part of the complex capacitance (C_r). f_{knee} is defined as the frequency at which C_r is half of the maximum capacitance reached at low frequency. The lower the value of f_{knee}, the longer it takes for ions to diffuse into the material [70]. For comparison, C_r was normalized by the capacitance at f = 0.01 Hz ($C_{0.01}$) and shown in Figure 8d as function of frequency. As expected, f_{knee} for OMC-CO_2-75 is about one order of magnitude higher than that of OMC-*pm*-4, evidence of significantly better ion diffusion into the CO_2-activated material. This rapid response of OMC-CO_2-75 would explain why, despite its higher O surface concentration than the KOH-activated material (Figure 5c and 5d), redox reactions are less likely to occur. In contrast, the slow diffusion of ions in the OMC-*pm*-4 material would allow sufficient time for the ions to react with the surface functionalities. This would result in the aforementioned electrolyte decomposition at the lowest I and the presence of pseudocapacitance contributions up to a relatively high current of 4 A g^{-1}. These EIS measurements are in agreement with the conclusions drawn from the GCD tests (Figure 8a).

In summary, the better performance of the CO_2-activated material compared to the KOH-activated counterpart can be attributed to key differences in their physicochemical properties, see Figure S9 for a direct comparison. As discussed in Section 3.1, hysteresis loops scanning analysis of the N_2 adsorption-desorption isotherms revealed that CO_2 activation of OMC resulted in a material with generally improved pore network connectivity. In addition, the

apparent water affinity constant of OMC-CO_2-75, calculated from the adsorption isotherms, is about 6 times higher than that of OMC-*pm*-4. The hydrophobic nature of KOH-activated materials could contribute to the diffusion problems arising from its low pore connectivity. This would explain the poor performance of the material at high charging rates, where ions from the aqueous electrolyte are unable to reach the narrower pores to form the EDL.

3.4.3. Comparison with literature

So far, a direct comparison of tannin-derived activated OMCs obtained by the same synthesis method has been performed. Therefore, it is possible that the observed differences in electrochemical performance, attributed to the different material properties resulting from the activation method used, are a particular case that occurs only for these tannin-derived materials. To clarify this, Figure 9 compares the electrochemical performance in the aqueous electrolyte H_2SO_4 of different KOH- and CO_2-activated materials. These materials were mostly obtained from phenolic precursors but also from other precursors such as polymers, pyrrole, sucrose, or biomass (see more details in Table S4). It is important to note that such a comparison remains challenging and needs to be considered carefully, as there are no standard conditions for the assessment of electrochemical performance at the laboratory scale. Data reports in the literature often differ on several test conditions such as cell type (2 or 3 electrodes), electrolyte concentration, potential window or carbon load (CL).

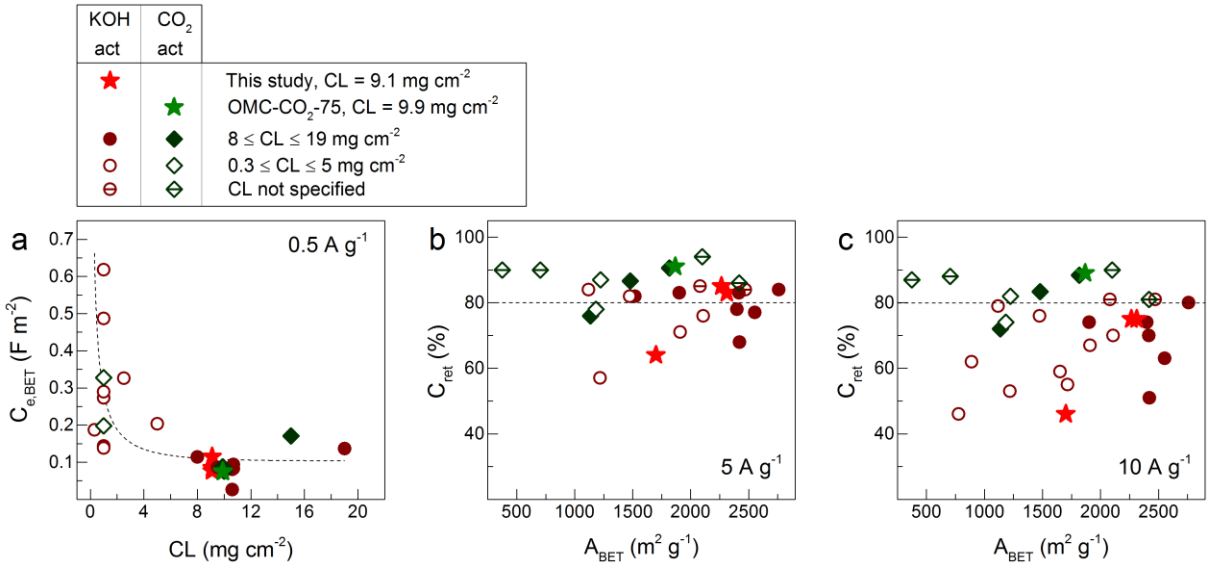

Figure 9. Electrochemical performance of KOH- and CO_2-ACs from this study compared to literature data [18,37,47,55–68]. (a) Specific electrode capacitance normalized by BET area ($C_{e,BET}$) as a function of carbon load (CL). (b, c) Capacitance retention (C_{ret}) as a function of BET area (A_{BET}) at 5 and 10 A g^{-1}; C_{ret} was calculated considering the capacitance at 0.5 A g^{-1} as the maximum (C_{ret} = 100%).

Among the test conditions, CL is known to significantly affect the performance of the materials and it has been shown that tests using thin electrodes with low CLs can lead to overestimation of capacitance and rate capability [37,39,71–73]. Such thin electrodes do not suffer from low mass transfer effects reducing their overall resistance and increasing their performance. To illustrate the effect of CL on SC performance, Figure 9a shows the values of specific electrode capacitance normalized by BET area ($C_{e,BET}$) of different KOH- and CO_2-activated carbon materials [18,37,47,55,56,58–65]. Indeed, a general trend is observed, where $C_{e,BET}$ increases drastically when CL decreases to values below 5 mg cm^{-2}.

Furthermore, care must be taken when comparing the C_{ret} values from different reports, since the maximum capacitance used as reference is not always obtained at the same charging rate, which can vary from 0.05 to 1 A g^{-1}. Therefore, Figure 9b and 9c show the capacitance retention at 5 and 10 A g^{-1} of the materials as a function of A_{BET} [18,37,47,55–68], all of these

values having been calculated considering the capacitance at 0.5 A g^{-1} as the maximum value. Figure 9b shows that at 5 A g^{-1}, most of the CO_2-ACs achieve retention values above 80 % and overall exhibit higher capacitance retentions than the KOH-ACs. As shown in Figure 9c, after doubling the applied current to 10 A g^{-1}, CO_2-ACs still retain more than 80 % of their capacitance. In contrast, C_{ret} of most KOH-ACs decreases to values below 75 % and down to 46 %, despite the fact that a large portion of them were tested using CLs ≤ 5 mg cm^{-2}, which generally leads to better rate capability [37,74]. Thus, it can be assumed that materials tested with low CLs would show even lower capacitance retentions at 10 A g^{-1} if they were tested with higher CLs, closer to those used in commercial devices.

This comparison indeed suggests that CO_2 activation produces materials with higher rate capability than KOH activation for tannin-derived carbons as well as for materials from a variety of precursors and with different morphologies and structures (see again Table S4). In view of the characterization carried out for the materials in this study, this superior performance of CO_2-ACs at higher charging rates would be a consequence of an appropriate combination of the material properties. Not only high surface area and pore volume are essential, but also good pore network connectivity and greater water affinity that enhance their performance in an aqueous electrolyte.

Finally, from a sustainability perspective, life-cycle assessments of the production of H_3PO_4-AC form olive-waste cake [75] and KOH-AC from energy crops (switchgrass and miscanthus) [76] and PET plastic bottles [77] have revealed that the environmental impact of these activation processes is mainly related to their toxicity to humans and water pollution. Recycling of activating agents can mitigate water pollution issues and reduce costs, but studies show that physical activation, by steam or CO_2, remains a more environmentally friendly and economically feasible process [75–78]. Although steam activation is widely used for the production of commercial ACs, it leads to the development of larger mesopores, $w >$

10 nm [79], which do not contribute to the performance when these ACs are used as SC electrodes [80]. Thus, given the electrochemical characterization shown in this study, and although further sustainability studies are needed, CO_2 activation appears to be a better choice than KOH as an activating agent to produce economically viable, high-rate capability SCs with low environmental impact.

Conclusion

This study shows that CO_2 is a better activating agent than KOH to produce high-rate capability supercapacitors (SCs) using an aqueous electrolyte. In addition, we demonstrate the utility of hysteresis loop scanning analysis of the N_2 adsorption-desorption isotherms and water adsorption at low relative pressures to explain the electrochemical performance of the materials. KOH physical mixing and impregnation of a tannin-derived ordered mesoporous carbon (OMC) were implemented prior to thermal treatment to produce activated materials, KOH-OMCs. A direct comparison of a KOH- and a CO_2-activated OMC with similar surface area revealed that the CO_2-OMC exhibited higher rate capabilities and faster ion diffusion than the KOH-OMC. The superior performance of the CO_2-OMC can be attributed to better pore network connectivity and approximately 6-fold higher water affinity than the KOH-OMC. A comparison with literature data showed that, although KOH activation is widely used to increase the surface area of carbon materials and achieve higher capacitance values, CO_2-ACs appear to exhibit an appropriate combination of textural properties, pore network connectivity, and water affinity that results in SCs with fast response and high capacitance retention at high charging rates. In addition, CO_2 activation also appears to be a more environmentally friendly and economically feasible choice than KOH activation for the production of ACs.

Acknowledgments

Jimena Castro-Gutiérrez gratefully acknowledges CONACYT-SENER for the grant awarded [601021/438978] to support her PhD studies, resulting in the work presented herein. This study was partly supported by the French PIA project "Lorraine Université d'Excellence" [reference ANR-15-IDEX-04-LUE], and the TALiSMAN project, funded by ERDF [2019-000214]. The authors particularly thank Philippe Gadonneix for his help in the laboratory and for the EA measurements.

References

[1] Lim E, Jo C, Lee J. A mini review of designed mesoporous materials for energy-storage applications: from electric double-layer capacitors to hybrid supercapacitors. Nanoscale 2016;8:7827–33. https://doi.org/10.1039/C6NR00796A.

[2] Herou S, Ribadeneyra MC, Madhu R, Araullo-Peters V, Jensen A, Schlee P, et al. Ordered mesoporous carbons from lignin: a new class of biobased electrodes for supercapacitors. Green Chem 2019;21:550–9. https://doi.org/10.1039/C8GC03497D.

[3] Vix-Guterl C, Frackowiak E, Jurewicz K, Friebe M, Parmentier J, Béguin F. Electrochemical energy storage in ordered porous carbon materials. Carbon 2005;43:1293–302. https://doi.org/10.1016/j.carbon.2004.12.028.

[4] Sanchez-Sanchez A, Izquierdo MT, Ghanbaja J, Medjahdi G, Mathieu S, Celzard A, et al. Excellent electrochemical performances of nanocast ordered mesoporous carbons based on tannin-related polyphenols as supercapacitor electrodes. J Power Sources 2017;344:15–24. https://doi.org/10.1016/j.jpowsour.2017.01.099.

[5] Moussa G, Hajjar-Garreau S, Taberna P-L, Simon P, Matei Ghimbeu C. Eco-Friendly Synthesis of Nitrogen-Doped Mesoporous Carbon for Supercapacitor Application. C 2018;4:20. https://doi.org/10.3390/c4020020.

[6] Feng S, Li W, Wang J, Song Y, Elzatahry AA, Xia Y, et al. Hydrothermal synthesis of ordered mesoporous carbons from a biomass-derived precursor for electrochemical capacitors. Nanoscale 2014;6:14657–61. https://doi.org/10.1039/C4NR05629A.

[7] Fierro V, Sánchez-Sánchez A, Celzard A. Tannins as Precursors of Supercapacitor Electrodes. In: Rincón-Mejía E, de las Heras A, editors. Sustainable Energy Technologies, Boca Raton, Florida, USA: CRC Press; 2018, p. 201–28.

[8] Castro-Gutiérrez J, Fierro V, Celzard A. Energy storage in supercapacitors: focus on tannin-derived carbon electrodes. Front Mater 2020;7:217. https://doi.org/10.3389/fmats.2020.00217.

[9] Zhang M, He L, Shi T, Zha R. Nanocasting and Direct Synthesis Strategies for Mesoporous Carbons as Supercapacitor Electrodes. Chem Mater 2018;30:7391–412. https://doi.org/10.1021/acs.chemmater.8b03345.

[10] Ma T-Y, Liu L, Yuan Z-Y. Direct synthesis of ordered mesoporous carbons. Chem Soc Rev 2013;42:3977–4003. https://doi.org/10.1039/C2CS35301F.

[11] Sevilla M, Mokaya R. Energy storage applications of activated carbons: supercapacitors and hydrogen storage. Energy Environ Sci 2014;7:1250–80. https://doi.org/10.1039/C3EE43525C.

[12] Gadipelli S, Howard CA, Guo J, Skipper NT, Zhang H, Shearing PR, et al. Superior Multifunctional Activity of Nanoporous Carbons with Widely Tunable Porosity: Enhanced Storage Capacities for Carbon-Dioxide, Hydrogen, Water, and Electric Charge. Adv Energy Mater 2020;10:1903649. https://doi.org/10.1002/aenm.201903649.
[13] Platek A, Nita C, Ghimbeu CM, Frąckowiak E, Fic K. Electrochemical capacitors operating in aqueous electrolyte with volumetric characteristics improved by sustainable templating of electrode materials. Electrochim Acta 2020;338:135788. https://doi.org/10.1016/j.electacta.2020.135788.
[14] Inagaki M, Konno H, Tanaike O. Carbon materials for electrochemical capacitors. J Power Sources 2010;195:7880–903. https://doi.org/10.1016/j.jpowsour.2010.06.036.
[15] Ciszewski M, Koszorek A, Radko T, Szatkowski P, Janas D. Review of the Selected Carbon-Based Materials for Symmetric Supercapacitor Application. J Electron Mater 2019;48:717–44. https://doi.org/10.1007/s11664-018-6811-7.
[16] Yoshida N, Hirota Y, Uchida Y, Asada T, Kobayashi N, Nishiyama N. Solvent-free synthesis and KOH activation of mesoporous carbons using resorcinol/Pluronic F127/hexamethylenetetramine mixture and their application to EDLC. Microporous Mesoporous Mater 2018;272:217–21. https://doi.org/10.1016/j.micromeso.2018.06.028.
[17] Lin G, Ma R, Zhou Y, Hu C, Yang M, Liu Q, et al. Three-dimensional interconnected nitrogen-doped mesoporous carbons as active electrode materials for application in electrocatalytic oxygen reduction and supercapacitors. J Colloid Interface Sci 2018;527:230–40. https://doi.org/10.1016/j.jcis.2018.05.020.
[18] Lu S, Song Y, Guo K, Chen X, Xu J, Zhao L. Effect of aqueous electrolytes on the electrochemical behaviors of ordered mesoporous carbon composites after KOH activation as supercapacitors electrodes. J Electroanal Chem 2018;818:58–67. https://doi.org/10.1016/j.jelechem.2018.04.025.
[19] Libich J, Máca J, Vondrák J, Čech O, Sedlaříková M. Supercapacitors: Properties and applications. J Energy Storage 2018;17:224–7. https://doi.org/10.1016/j.est.2018.03.012.
[20] Qu D. Studies of the activated carbons used in double-layer supercapacitors. J Power Sources 2002;109:403–11. https://doi.org/10.1016/S0378-7753(02)00108-8.
[21] Liu L, Tan S (Johnathan), Horikawa T, Do DD, Nicholson D, Liu J. Water adsorption on carbon - A review. Adv Colloid Interface Sci 2017;250:64–78. https://doi.org/10.1016/j.cis.2017.10.002.
[22] Vartapetyan RS, Voloshchuk AM. The mechanism of the adsorption of water molecules on carbon adsorbents. Russ Chem Rev 1995;64:985–1001. https://doi.org/10.1070/RC1995v064n11ABEH000189.
[23] Stoeckli F. Water adsorption in activated carbons of various degrees of oxidation described by the Dubinin equation. Carbon 2002;40:969–71. https://doi.org/10.1016/S0008-6223(02)00087-8.
[24] Pires JO, Pinto MSL, Carvalho A, Carvalho MBD. Assessment of Hydrophobic-Hydrophilic Properties of Microporous Materials from Water Adsorption Isotherms. Adsorption 2003;9:303–9.
[25] Walker PL, Janov J. Hydrophilic oxygen complexes on activated graphon. J Colloid Interface Sci 1968;28:449–58. https://doi.org/10.1016/0021-9797(68)90076-3.
[26] Zeng Y, Prasetyo L, Nguyen VT, Horikawa T, Do DD, Nicholson D. Characterization of oxygen functional groups on carbon surfaces with water and methanol adsorption. Carbon 2015;81:447–57. https://doi.org/10.1016/j.carbon.2014.09.077.
[27] Castro-Gutiérrez J, Sanchez-Sanchez A, Ghanbaja J, Díez N, Sevilla M, Celzard A, et al. Synthesis of perfectly ordered mesoporous carbons by water-assisted mechanochemical self-assembly of tannin. Green Chem 2018;20:5123–32. https://doi.org/10.1039/c8gc02295j.
[28] Salinas-Torres D, Ruiz-Rosas R, Morallón E, Cazorla-Amorós D. Strategies to Enhance the Performance of Electrochemical Capacitors Based on Carbon Materials. Front Mater 2019;6:115. https://doi.org/10.3389/fmats.2019.00115.
[29] Inagaki M, Toyoda M, Soneda Y, Morishita T. Nitrogen-doped carbon materials. Carbon 2018;132:104–40. https://doi.org/10.1016/j.carbon.2018.02.024.

[30] Benzigar MR, Talapaneni SN, Joseph S, Ramadass K, Singh G, Scaranto J, et al. Recent advances in functionalized micro and mesoporous carbon materials: synthesis and applications. Chem Soc Rev 2018;47:2680–721. https://doi.org/10.1039/C7CS00787F.
[31] Gao Z, Zhang Y, Song N, Li X. Biomass-derived renewable carbon materials for electrochemical energy storage. Mater Res Lett 2017;5:69–88. https://doi.org/10.1080/21663831.2016.1250834.
[32] González A, Goikolea E, Barrena JA, Mysyk R. Review on supercapacitors: Technologies and materials. Renew Sustain Energy Rev 2016;58:1189–206. https://doi.org/10.1016/j.rser.2015.12.249.
[33] Wang Y, Song Y, Xia Y. Electrochemical capacitors: mechanism, materials, systems, characterization and applications. Chem Soc Rev 2016;45:5925–50. https://doi.org/10.1039/C5CS00580A.
[34] Dutta S, Bhaumik A, Wu KC-W. Hierarchically porous carbon derived from polymers and biomass: effect of interconnected pores on energy applications. Energy Environ Sci 2014;7:3574–92. https://doi.org/10.1039/C4EE01075B.
[35] Zhai Y, Dou Y, Zhao D, Fulvio PF, Mayes RT, Dai S. Carbon Materials for Chemical Capacitive Energy Storage. Adv Mater 2011;23:4828–50. https://doi.org/10.1002/adma.201100984.
[36] Zhang LL, Zhao XS. Carbon-based materials as supercapacitor electrodes. Chem Soc Rev 2009;38:2520. https://doi.org/10.1039/b813846j.
[37] Castro-Gutiérrez J, Díez N, Sevilla M, Izquierdo MT, Ghanbaja J, Celzard A, et al. High-Rate Capability of Supercapacitors Based on Tannin-Derived Ordered Mesoporous Carbons. ACS Sustainable Chem Eng 2019;7:17627–35. https://doi.org/10.1021/acssuschemeng.9b03407.
[38] Thommes M, Kaneko K, Neimark AV, Olivier JP, Rodriguez-Reinoso F, Rouquerol J, et al. Physisorption of gases, with special reference to the evaluation of surface area and pore size distribution (IUPAC Technical Report). Pure Appl Chem 2015;87. https://doi.org/10.1515/pac-2014-1117.
[39] Stoller MD, Ruoff RS. Best practice methods for determining an electrode material's performance for ultracapacitors. Energy Environ Sci 2010;3:1294. https://doi.org/10.1039/c0ee00074d.
[40] Sevilla M, Ferrero GA, Diez N, Fuertes AB. One-step synthesis of ultra-high surface area nanoporous carbons and their application for electrochemical energy storage. Carbon 2018;131:193–200. https://doi.org/10.1016/j.carbon.2018.02.021.
[41] Lozano-Castelló D, Calo JM, Cazorla-Amorós D, Linares-Solano A. Carbon activation with KOH as explored by temperature programmed techniques, and the effects of hydrogen. Carbon 2007;45:2529–36. https://doi.org/10.1016/j.carbon.2007.08.021.
[42] Castro-Gutiérrez J, De Oliveira Jardim E, Canevesi RLS, Silvestre-Albero J, Kriesten M, Thommes M, et al. Molecular sieving of linear and branched C6 alkanes by tannin-derived carbons. Carbon 2021;174:413–22. https://doi.org/10.1016/j.carbon.2020.12.061.
[43] Illán-Gómez MJ, García-García A, Salinas-Martínez de Lecea C, Linares-Solano A. Activated Carbons from Spanish Coals. 2. Chemical Activation. Energy Fuels 1996;10:1108–14. https://doi.org/10.1021/ef950195+.
[44] Jibril BY, Al-Maamari RS, Hegde G, Al-Mandhary N, Houache O. Effects of feedstock pre-drying on carbonization of KOH-mixed bituminous coal in preparation of activated carbon. J Anal Appl Pyrolysis 2007;80:277–82. https://doi.org/10.1016/j.jaap.2007.03.003.
[45] Cychosz KA, Guillet-Nicolas R, García-Martínez J, Thommes M. Recent advances in the textural characterization of hierarchically structured nanoporous materials. Chem Soc Rev 2017;46:389–414. https://doi.org/10.1039/C6CS00391E.
[46] Cimino R, Cychosz KA, Thommes M, Neimark AV. Experimental and theoretical studies of scanning adsorption–desorption isotherms. Colloids Surf A Physicochem 2013;437:76–89. https://doi.org/10.1016/j.colsurfa.2013.03.025.
[47] Castro-Gutiérrez J, Díez N, Sevilla M, Izquierdo MT, Celzard A, Fierro V. Model carbon materials derived from tannin to assess the importance of pore connectivity in supercapacitors. Renew Sust Energ Rev 2021;151:111600. https://doi.org/10.1016/j.rser.2021.111600.

[48] Thommes M, Cychosz KA. Physical adsorption characterization of nanoporous materials: progress and challenges. Adsorption 2014;20:233–50. https://doi.org/10.1007/s10450-014-9606-z.
[49] Nguyen VT, Horikawa T, Do DD, Nicholson D. Water as a potential molecular probe for functional groups on carbon surfaces. Carbon 2014;67:72–8. https://doi.org/10.1016/j.carbon.2013.09.057.
[50] Furmaniak S, Gauden PA, Terzyk AP, Rychlicki G. Water adsorption on carbons — Critical review of the most popular analytical approaches. Adv Colloid Interface Sci 2008;137:82–143. https://doi.org/10.1016/j.cis.2007.08.001.
[51] Striolo A, Chialvo AA, Cummings PT, Gubbins KE. Water Adsorption in Carbon-Slit Nanopores. Langmuir 2003;19:8583–91. https://doi.org/10.1021/la0347354.
[52] Striolo A, Chialvo AA, Cummings PT, Gubbins KE. Simulated water adsorption in chemically heterogeneous carbon nanotubes. The Journal of Chemical Physics 2006;124:074710. https://doi.org/10.1063/1.2171349.
[53] Furmaniak S, Gauden PA, Terzyk AP, Rychlicki G, Wesołowski RP, Kowalczyk P. Heterogeneous Do–Do model of water adsorption on carbons. Journal of Colloid and Interface Science 2005;290:1–13. https://doi.org/10.1016/j.jcis.2005.07.043.
[54] Zuliani JE, Caguiat JN, Kirk DW, Jia CQ. Considerations for consistent characterization of electrochemical double-layer capacitor performance. J Power Sources 2015;290:136–43. https://doi.org/10.1016/j.jpowsour.2015.04.019.
[55] Pérez-Rodríguez S, Pinto O, Izquierdo MT, Segura C, Poon PS, Celzard A, et al. Upgrading of pine tannin biochars as electrochemical capacitor electrodes. J Colloid Interface Sci 2021;601:863–76. https://doi.org/10.1016/j.jcis.2021.05.162.
[56] Sanchez-Sanchez A, Izquierdo MT, Medjahdi G, Ghanbaja J, Celzard A, Fierro V. Ordered mesoporous carbons obtained by soft-templating of tannin in mild conditions. Microporous Mesoporous Mater 2018;270:127–39. https://doi.org/10.1016/j.micromeso.2018.05.017.
[57] Ferrero GA, Fuertes AB, Sevilla M. N-doped porous carbon capsules with tunable porosity for high-performance supercapacitors. J Mater Chem A 2015;3:2914–23. https://doi.org/10.1039/C4TA06022A.
[58] Wang Z, Zhou M, Chen H, Jiang J, Guan S. Hierarchical Activated Mesoporous Phenolic-Resin-Based Carbons for Supercapacitors. Chem Asian J 2014;9:2789–97. https://doi.org/10.1002/asia.201402338.
[59] Zhang K, Ang BT, Zhang LL, Zhao XS, Wu J. Pyrolyzed graphene oxide/resorcinol-formaldehyde resin composites as high-performance supercapacitor electrodes. J Mater Chem 2011;21:2663. https://doi.org/10.1039/c0jm02850a.
[60] Barranco V, Lillo-Rodenas MA, Linares-Solano A, Oya A, Pico F, Ibañez J, et al. Amorphous Carbon Nanofibers and Their Activated Carbon Nanofibers as Supercapacitor Electrodes. J Phys Chem C 2010;114:10302–7. https://doi.org/10.1021/jp1021278.
[61] Li M, Chang X, Han X, Yin W, Ren M. Resorcinol-formaldehyde resin based porous carbon materials with yolk-shell structure for high-performance supercapacitors. Synth Met 2016;219:67–75. https://doi.org/10.1016/j.synthmet.2016.05.011.
[62] Lota G, Centeno TA, Frackowiak E, Stoeckli F. Improvement of the structural and chemical properties of a commercial activated carbon for its application in electrochemical capacitors. Electrochim Acta 2008;53:2210–6. https://doi.org/10.1016/j.electacta.2007.09.028.
[63] Wang C, Liu T. Activated carbon materials derived from liquefied bark-phenol formaldehyde resins for high performance supercapacitors. RSC Adv 2016;6:105540–9. https://doi.org/10.1039/C6RA20373F.
[64] Chen Z, Zhuo H, Hu Y, Zhong L, Peng X, Jing S, et al. Self-Biotemplate Preparation of Hierarchical Porous Carbon with Rational Mesopore Ratio and High Oxygen Content for an Ultrahigh Energy-Density Supercapacitor. ACS Sustain Chem Eng 2018;6:7138–50. https://doi.org/10.1021/acssuschemeng.8b01159.
[65] Wickramaratne NP, Xu J, Wang M, Zhu L, Dai L, Jaroniec M. Nitrogen Enriched Porous Carbon Spheres: Attractive Materials for Supercapacitor Electrodes and CO_2 Adsorption. Chem Mater 2014;26:2820–8. https://doi.org/10.1021/cm5001895.

[66] Wei L, Yushin G. Electrical double layer capacitors with activated sucrose-derived carbon electrodes. Carbon 2011;49:4830–1838. https://doi.org/10.1016/j.carbon.2011.07.003.
[67] Ra EJ, Raymundo-Piñero E, Lee YH, Béguin F. High power supercapacitors using polyacrylonitrile-based carbon nanofiber paper. Carbon 2009;47:2984–92. https://doi.org/10.1016/j.carbon.2009.06.051.
[68] Hasegawa G. Monolithic Electrode for Electric Double-Layer Capacitors Based on Macro/Meso/Microporous S-Containing Activated Carbon with High Surface Area. Studies on Porous Monolithic Materials Prepared via Sol–Gel Processes, Tokyo: Springer Japan; 2013, p. 79–89. https://doi.org/10.1007/978-4-431-54198-1_6.
[69] Gyenes B, Stevens DA, Chevrier VL, Dahn JR. Understanding Anomalous Behavior in Coulombic Efficiency Measurements on Li-Ion Batteries. J Electrochem Soc 2015;162:A278–83. https://doi.org/10.1149/2.0191503jes.
[70] Beguin F, Frackowiak E, editors. Supercapacitors: Materials, Systems, and Applications. Weinheim, Germany: John Wiley & Sons, Ltd; 2013.
[71] Xie J, Yang P, Wang Y, Qi T, Lei Y, Li CM. Puzzles and confusions in supercapacitor and battery: Theory and solutions. J Power Sources 2018;401:213–23. https://doi.org/10.1016/j.jpowsour.2018.08.090.
[72] Gogotsi Y, Simon P. True Performance Metrics in Electrochemical Energy Storage. Science 2011;334:917–8. https://doi.org/10.1126/science.1213003.
[73] Chmiola J, Largeot C, Taberna PL, Simon P, Gogotsi Y. Monolithic Carbide-Derived Carbon Films for Micro-Supercapacitors. Science 2010;328:480–3. https://doi.org/10.1126/science.1184126.
[74] Hu L, Choi JW, Yang Y, Jeong S, La Mantia F, Cui L-F, et al. Highly conductive paper for energy-storage devices. Proc Natl Acad Sci USA 2009;106:21490–4. https://doi.org/10.1073/pnas.0908858106.
[75] Hjaila K, Baccar R, Sarrà M, Gasol CM, Blánquez P. Environmental impact associated with activated carbon preparation from olive-waste cake via life cycle assessment. J Environ Manage 2013;130:242–7. https://doi.org/10.1016/j.jenvman.2013.08.061.
[76] Wang Y, Wang J, Zhang X, Bhattacharyya D, Sabolsky EM. Quantifying Environmental and Economic Impacts of Highly Porous Activated Carbon from Lignocellulosic Biomass for High-Performance Supercapacitors. Energies 2022;15:351. https://doi.org/10.3390/en15010351.
[77] Yuan X, Kumar NM, Brigljević B, Li S, Deng S, Byun M, et al. Sustainability-inspired upcycling of waste polyethylene terephthalate plastic into porous carbon for CO_2 capture. Green Chem 2022:10.1039.D1GC03600A. https://doi.org/10.1039/D1GC03600A.
[78] Ng C, Marshall WE, Rao RM, Bansode RR, Losso JN. Activated carbon from pecan shell: process description and economic analysis. Ind Crops Prod 2003;17:209–17. https://doi.org/10.1016/S0926-6690(03)00002-5.
[79] Celzard A, Fierro V. "Green", innovative, versatile and efficient carbon materials from polyphenolic plant extracts. Carbon 2020;167:792–815. https://doi.org/10.1016/j.carbon.2020.05.053.
[80] Pandolfo AG, Hollenkamp AF. Carbon properties and their role in supercapacitors. J Power Sources 2006;157:11–27. https://doi.org/10.1016/j.jpowsour.2006.02.065.